

Machine Learning-Based Seismic Fragility Analysis of Large-Scale Steel Buckling Restrained Brace Frames

Baoyin Sun^{1,2}, Yantai Zhang³ and Caigui Huang^{4,*}

¹Key Laboratory of Earthquake Engineering and Engineering Vibration, Institute of Engineering Mechanics, China Earthquake Administration, Harbin, 150080, China

²Faculty of Infrastructure Engineering, Dalian University of Technology, Dalian, 116024, China

³College of Civil Engineering, Nanjing Forestry University, Nanjing, 210037, China

⁴School of Architecture and Civil Engineering, Xiamen University, Xiamen, 361005, China

*Corresponding Author: Caigui Huang. Email: huangcaigui@stu.xmu.edu.cn

Received: 18 January 2020; Accepted: 28 June 2020

Abstract: Steel frames equipped with buckling restrained braces (BRBs) have been increasingly applied in earthquake-prone areas given their excellent capacity for resisting lateral forces. Therefore, special attention has been paid to the seismic risk assessment (SRA) of such structures, e.g., seismic fragility analysis. Conventional approaches, e.g., nonlinear finite element simulation (NFES), are computationally inefficient for SRA analysis particularly for large-scale steel BRB frame structures. In this study, a machine learning (ML)-based seismic fragility analysis framework is established to effectively assess the risk to structures under seismic loading conditions. An optimal artificial neural network model can be trained using calculated damage and intensity measures, a technique which will be used to compute the fragility curves of a steel BRB frame instead of employing NFES. Numerical results show that a highly efficient instantaneous failure probability assessment can be made with the proposed framework for realistic large-scale building structures.

Keywords: Machine learning; Monte Carlo simulation; regression method; fragility analysis; buckling restrained braces

1 Introduction

Steel frames equipped with the buckling restrained braces (BRBs) are gaining increasing popularity and have wide applications in new structures [1–3] or for retrofitting existing ones [4] given their excellent lateral force resistance. Fragility analysis plays an essential role for the seismic risk assessment (SRA) of the steel BRB structures in earthquake-prone areas [5]. According to the performance-based structural design method, the damage limit state, D , of a structure under seismic excitations can be divided into several levels, e.g., negligible, light, moderate, and severe damage states [5]. The probability of failure can be expressed as $P_f = P[DM \geq D]$, where DM indicates the damage measure. Considering that the intensity measure (IM) of a given



This work is licensed under a Creative Commons Attribution 4.0 International License, which permits unrestricted use, distribution, and reproduction in any medium, provided the original work is properly cited.

ground motion may be an uncertain value, e.g., the peak ground acceleration (PGA) or spectral acceleration (Sa), the conditional probability of failure can be modified as [6],

$$P_f = P[DM \geq D] = \sum_{All\ x} P[DM \geq D | IM = x] P[IM = x] \quad (1)$$

where $P[DM \geq D | IM = x]$ indicates the fragility that suggests the failure probability under the ground motion IM level x , and $P[IM = x]$ expresses the annual occurrence probabilities of the specific level x of an earthquake motion.

The Monte Carlo Simulation (MCS) based on the nonlinear finite element simulation (NFES) [7] is one of the most accurate and popular techniques. However, the MCS is computationally prohibitive because of its tremendous time cost, especially for realistic large-scale structures. Consequently, some approximate regression methods, such as the least-squares [8] and empirical regression methods [9], are commonly used to compute the fragility curve by utilizing the limited data of structural responses. Among them, the empirical regression (denoted as *Reg*) method is slightly more popular and expresses the fragility curve in the form of two-parameter lognormal distribution functions [10].

Given the epistemic uncertainties of structures and the aleatory uncertainties of earthquakes, numerous repeated simulations may be necessary to perform structural reliability or fragility analysis using the MCS or the *Reg* method. Therefore, conducting instantaneous SRA of realistic large-scale structures is problematic for researchers and engineers.

In the last few years, machine learning (ML) has become a powerful tool that supplanted conventional finite element (FE) approaches for repeated computation. The artificial neural network (ANN), an ML approach, has various applications in the reliability analysis of civil structures [11–23]. ML may also be extensively used in the fragility analysis of structural SRAs [24–32]. The basic idea of ML involves several steps. First, the actual DM of a structure under seismic loadings is calculated according to the NFES, and appropriate intensity measures (IMs) are selected to characterize the ground motion. Second, an optimal ML (e.g., the ANN) model is trained using the $IMs-DM$ data. Finally, the fragility curve of the structure can be predicted according to the ANN model. The main concerns focus on the selection of the IMs and predicted uncertainties of the ML (or ANN) model. For the IM selection, more than one IM is needed to represent the ground motion because the random earthquake process cannot be sufficiently characterized by any single seismic IM , such as the PGA, peak ground velocity (PGV), and SA. However, the ANN model will be overfitted if given too many selected IMs and will become complex if these selected IMs have substantial correlation with one another. A parametric study was conducted to select the suitable combination of IMs that leads to close predictions of the demand [28] but ignored the correlation among these selected IMs and that between the IM and DM . A wrapper approach based on the genetic algorithm can be employed to select the optimal set that maximizes ANN representation accuracy [27], for which the correlation between the selected IMs is considered. Another filter approach based on the semi-partial correlation coefficient is proposed to consider the independent correlation between the IM and DM [32]. For the predicted uncertainties of the ML (or ANN) model, the input and output randomness, as well as the effect of data size on the accuracy of the ANN model, are studied [27]. These uncertainties are investigated in relation to the fragility analysis of nuclear power plants [32].

In this paper, an ML-based seismic fragility analysis framework is proposed to instantaneous assess the failure probability of a realistic large-scale 48-story steel BRB frame under excitations.

The suggested framework is introduced in Section 2. The numerical results are presented and discussed in Section 3. Conclusions are provided in Section 4.

2 ML-Based Seismic Fragility Analysis Framework

As depicted in Fig. 1, the proposed ML-based seismic fragility analysis framework consists of three parts:

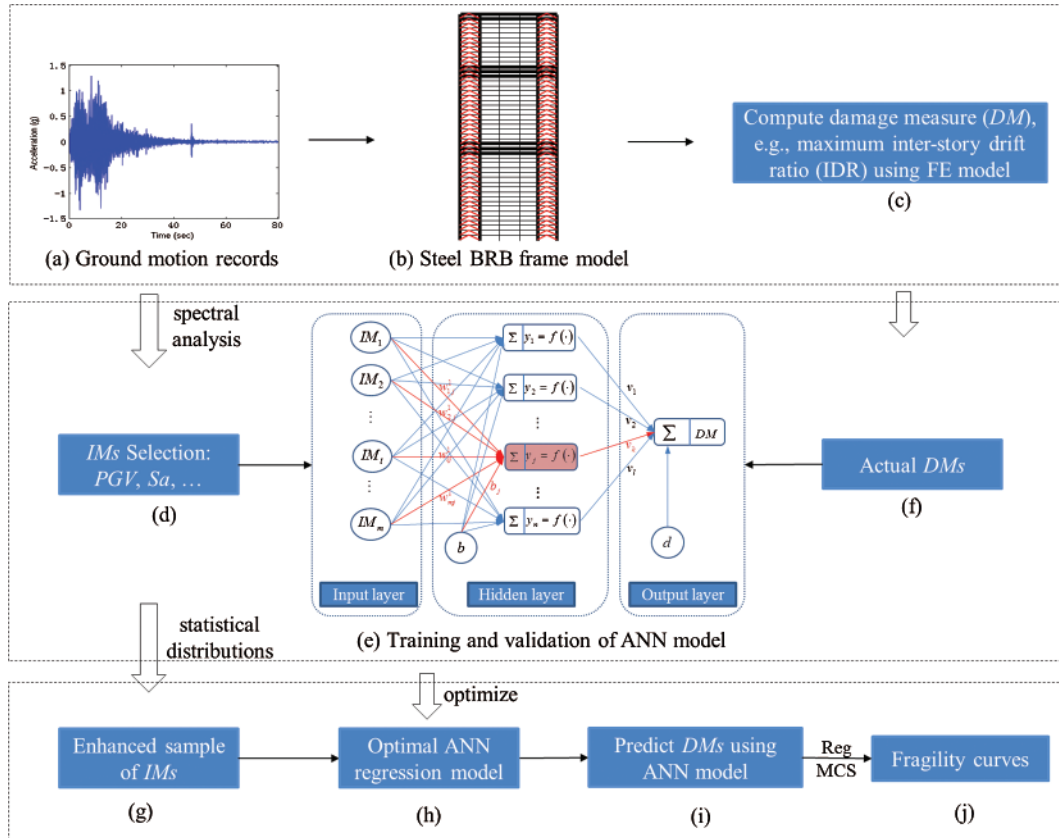


Figure 1: The ML-based seismic fragility analysis framework

- (I) NFES. A relatively large number of ground motion records are selected, the FE model of the steel BRB frame is developed, and the actual DMs of the structure are computed under these selected seismic excitations, (Figs. 1a–1c);
- (II) ANN regression model construction. The most relevant IMs are selected with the DM , and the IMs - DM data are used to train the ANN model (Figs. 1d–1f);
- (III) ML-based seismic fragility predictions. According to the statistical distributions of the selected IMs , an extended sample data of the IMs is obtained. Then, the optimal ANN model established in Part (II) can be used to predict the DM . Finally, the fragility curves of the steel BRB frame at various performance state limits can be calculated using the MCS or *Reg* method (Figs. 1g–1j).

This section is organized as follows. Section 2.1 introduces the structure model and presents the input ground motions. Section 2.2 explains the selection of the IMs and the training and validation of the ANN model. Section 2.3 demonstrates the sampling methods of the IMs and the prediction of the fragility curves.

2.1 NFES

2.1.1 Structure Model

This study conducts fragility analysis of a 48-story steel BRB frame. The structure is designed according to the Chinese Code for Seismic Design of Buildings GB50011-2010 [33], which consists of five-bay in the North–South and East–West directions with a span length of 8 m. Each story of the frame is 4 m in height. The building stands at 192 m. The concrete slabs of each floor and the roof are both 0.12 m in thickness. The elevation and plan views are shown in Fig. 2. The frame consists of mega columns, mega beams, secondary columns, secondary beams, mega-column beams, mega-column braces, and mega-beam braces (Figs. 2a and 2b). All columns and braces are of box sections (denoted as *B-type*), whereas all beams are of *I-type* sections. Three strength stories are designed and located at Floors 19–20, 36–37, and 48 (Fig. 2c). The section geometries and material of all components are given in Tab. 1.

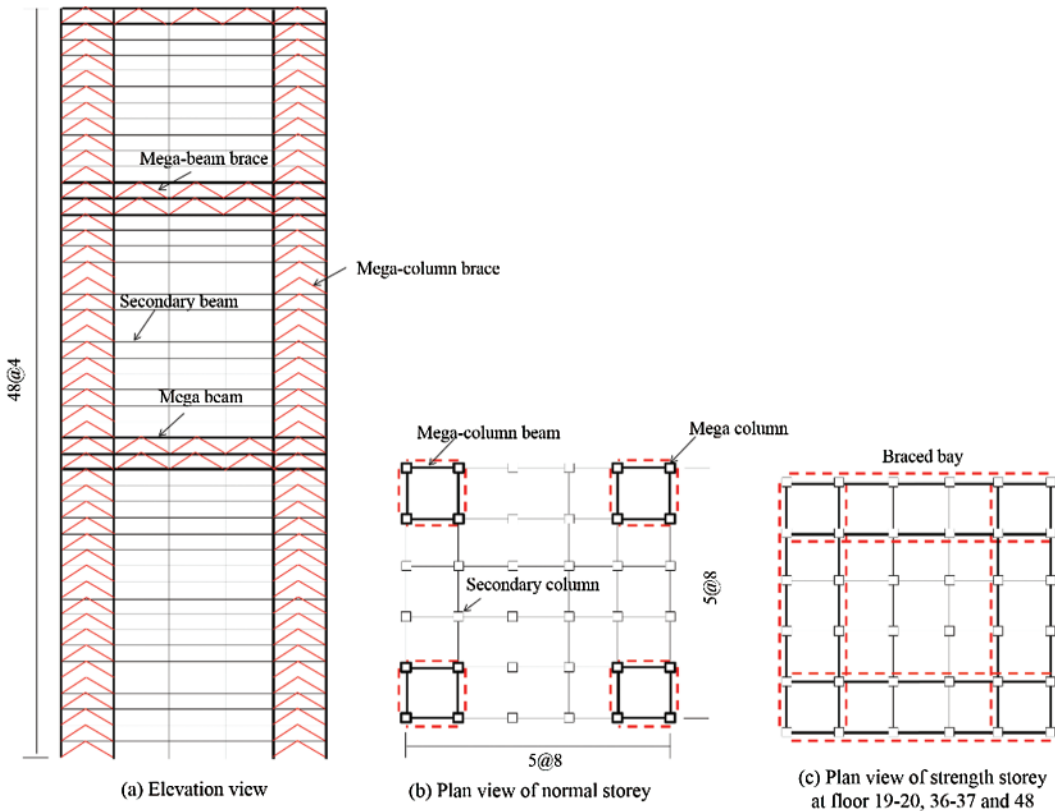


Figure 2: Elevation and plan views of 48-story steel BRB frame

The live load applied on each slab is 2.0 kN/m², the self-weight dead loads on each slab and the roof are 3.5 kN/m², and the roof has an additional dead load of 3.32 kN/m². The frame is

located in an earthquake-prone region with seismic fortification intensity 8 (0.2 g), site soil class II and design Group 1. The damping ratio of the structure under an 8-degree rare earthquake is taken as 0.02.

Table 1: Section geometries and materials of structural components (units: m)

Component	Floor	Section geometry	Material
Mega column	1–12	<i>B-type</i> $0.9 \times 0.9 \times 0.065 \times 0.065$	Q345
Mega column	13–24	<i>B-type</i> $0.9 \times 0.9 \times 0.04 \times 0.04$	
Secondary column	1–24	<i>B-type</i> $0.8 \times 0.8 \times 0.06 \times 0.06$	
Mega column	25–36	<i>B-type</i> $0.08 \times 0.8 \times 0.04 \times 0.04$	Q235
Mega column	37–48	<i>B-type</i> $0.7 \times 0.7 \times 0.03 \times 0.03$	
Secondary column	25–48	<i>B-type</i> $0.75 \times 0.75 \times 0.05 \times 0.05$	
Mega beam	1–48	<i>I-type</i> $0.8 \times 0.3 \times 0.019 \times 0.035$	
Secondary beam	1–48	<i>I-type</i> $0.692 \times 0.3 \times 0.013 \times 0.02$	
Mega-column beam	1–48	<i>I-type</i> $0.7 \times 0.3 \times 0.013 \times 0.024$	
Mega-column brace	1–24	<i>B-type</i> $0.25 \times 0.25 \times 0.018 \times 0.018$	
Mega-column brace	25–48	<i>B-type</i> $0.25 \times 0.25 \times 0.014 \times 0.014$	
Mega-beam brace	19–20	<i>B-type</i> $0.35 \times 0.35 \times 0.02 \times 0.02$	
Mega-beam brace	36–37,48	<i>B-type</i> $0.35 \times 0.35 \times 0.018 \times 0.018$	
Slab	1–48	$40 \times 40 \times 0.12$	C30

The BRB frame structure is analyzed using an open source software platform, OpenSees [34,35]. During the seismic analysis of the frame under earthquake loads, each column or beam component is modeled by using an Euler–Bernoulli fiber element with five Gauss points, where the uniaxial behaviors of steel fiber is simulated by using a uniaxial Giuffre–Menegotto–Pinto (GMP) model [34,36]. Moreover, the BRB component is simulated by employing a truss element, for which the uniaxial stress–strain relationship is computed by utilizing the GMP model. The beam–column connections are assumed to be rigid and the mass is regarded as concentrated at the beam–column joints. The first five periods and frequencies of the steel BRB frame are given in Tab. 2.

In the transient analysis, a Newmark- β integration scheme is employed with the parameters $\gamma = 0.5$ and $\beta = 0.25$, and the Rayleigh damping is assumed to have a damping ratio of 0.02 that corresponds to the first and second frequencies (1.29 and 4.14 Hz) in the seismic action direction (i.e., N–S direction). A tolerance of 1.0 e-5 mm on the norm of the incremental displacement is employed as the convergence criterion in the nonlinear iterative computation.

Table 2: First five periods and frequencies in the N–S direction of the SMF-BRB structure

Order	1	2	3	4	5
Period (s)	$T_1 = 4.88$	$T_2 = 1.52$	$T_3 = 0.77$	$T_4 = 0.50$	$T_5 = 0.36$
Frequency (rad/s)	$f_1 = 1.29$	$f_2 = 4.14$	$f_3 = 8.21$	$f_4 = 12.46$	$f_5 = 17.32$

2.1.2 Input Ground Motions

To obtain the *DM* data used for training the ANN model, a 48-story steel BRB frame is analyzed under a suite of 60 Los Angeles ground motion records in the SAC steel research project [37]. Detailed information of all ground motions is presented in Tab. 3. The magnitude range is from 5.7 to 7.7 and the source-to-site distance of the selected record ranges from 1 km to 107 km. These 60 records are divided into three groups in terms of the probability of exceedance: the first, middle, and last 20 ground motion records for 50 years are respectively represented as 10%, 2%, and 50%.

2.2 ANN Regression Model Construction

2.2.1 IM Selection

Given that the input earthquake motion is a random process, establishing a clear and simple relationship between the input and output *DMs* is difficult. Consequently, some *IMs* that represent the earthquake motion must be selected to describe the relationship. Characterizing seismic motion generally requires more than one *IM* [39]. Tab. 4 lists seven commonly used *IMs*, i.e., the *PGA*, *PGV*, peak ground displacement (*PGD*), *Sa*, average spectral acceleration (*ASA*), cumulative absolute velocity (*CAV*), arias intensity (*Ia*). Note that increasing the number of selected *IMs* will enhance the complexity of the ANN model and may even lead to a risk of overfitting. Therefore, selecting the most relevant *IMs* with the *DM* to train the ANN regression model is crucial.

As these *IMs* may be highly related to one another, conventional correlations are unsuitable for selecting the most relevant *IMs* with the *DM*. In this study, a filter approach on the basis of semi-partial correlation coefficients (SPCCs) is used to select the most relevant *IMs* [32], for which the independent correlation between any *IM* and *DM* can be accurately measured after controlling for (i.e., “partialling” out) the effects of the other six *IMs*. Tab. 5 and present the correlation coefficients and SPCCs between the logarithms of *IMs* and *DM*. *IM*₅ has the largest correlation coefficient (larger than 0.9) with the *DM* and a very small SPCC, whereas *IM*₃ (*PGD*) has the second largest correlation but the smallest SPCC (Tabs. 5 and 6). According to the correlation coefficients in Tab. 5, *IM*₂, *IM*₃, *IM*₄, and *IM*₅ are the most relevant *IMs* with the *DM*, whereas *IM*₂ and *IM*₄ (Tab. 6) are the most relevant ones quantified by the SPCCs. Therefore, *IM*₂ and *IM*₄ will be adopted to train the ANN model in the following simulation.

2.2.2 Training and Validation of the ANN Model

Subsequently, the ANN model can be constructed by using the *IMs-DM* data which consists of an input layer, hidden layer, and output layer (Fig. 3).

The hidden layer contains *n* independent neurons (or nodes), and each node receives all input *IMs* from the input layer and computes the output, thereby yielding

$$y_j = f \left(\sum_{i=1}^m w_{ij} IM_i + b_j \right), \quad j = 1, \dots, n \quad (2)$$

where *IM*_{*i*} is the *i*th input variable, *m* is the number of *IMs*, *y_j* is the output of the *j*th neuron in the hidden layer, *w_{ij}* is the weight coefficient contributed by the *IM*_{*i*} to the output *y_j*, *b_j* is the bias of the *j*th neuron in the hidden layer, and *f* is the activation function. The choice of the activation function plays an important role in the construction of the ANN. Activation functions occur as linear and nonlinear types. A nonlinear activation function with the sigmoid function as an example is expressed as

Table 3: Summary of selected ground motions [38]

Probability of exceedance	SAC name	Earthquake location	Magnitude	Distance (km)	PGA (g)
10% in 50 years	LA01	El Centro	6.9	10.0	0.461
	LA02	El Centro	6.9	10.0	0.676
	LA03	Imperial Valley	6.5	4.1	0.394
	LA04	Imperial Valley	6.5	4.1	0.488
	LA05	Imperial Valley	6.5	1.2	0.302
	LA06	Imperial Valley	6.5	1.2	0.235
	LA07	Landers, Barstow	7.3	36.0	0.421
	LA08	Landers, Barstow	7.3	36.0	0.426
	LA09	Landers, Yermo	7.3	25.0	0.520
	LA10	Landers, Yermo	7.3	25.0	0.361
	LA11	Loma Prieta, Gilroy	7	12.0	0.666
	LA12	Loma Prieta, Gilroy	7	12.0	0.970
	LA13	Northridge, Newhall	6.7	6.7	0.679
	LA14	Northridge, Newhall	6.7	6.7	0.658
	LA15	Northridge, Rinaldi RS	6.7	7.5	0.534
	LA16	Northridge, Rinaldi RS	6.7	7.5	0.580
	LA17	Northridge, Sylmar	6.7	6.4	0.570
	LA18	Northridge, Sylmar	6.7	6.4	0.818
	LA19	North Palm Springs	6	6.7	1.020
	LA20	North Palm Springs	6	6.7	0.987
2% in 50 years	LA21	Kobe	6.9	3.4	1.284
	LA22	Kobe	6.9	3.4	0.921
	LA23	Loma Prieta	7	3.5	0.418
	LA24	Loma Prieta	7	3.5	0.473
	LA25	Northridge	6.7	7.5	0.869
	LA26	Northridge	6.7	7.5	0.944
	LA27	Northridge	6.7	6.4	0.927
	LA28	Northridge	6.7	6.4	1.331
	LA29	Tabas	7.4	1.2	0.810
	LA30	Tabas	7.4	1.2	0.992
	LA31	Elysian Park	7.1	17.5	1.297
	LA32	Elysian Park	7.1	17.5	1.187
	LA33	Elysian Park	7.1	10.7	0.783
	LA34	Elysian Park	7.1	10.7	0.681
	LA35	Elysian Park	7.1	11.2	0.993
	LA36	Elysian Park	7.1	11.2	1.101
	LA37	Palos Verdes	7.1	1.5	0.712
	LA38	Palos Verdes	7.1	1.5	0.777
	LA39	Palos Verdes	7.1	1.5	0.501
	LA40	Palos Verdes	7.1	1.5	0.626

(Continued)

Table 3 (continued).

Probability of exceedance	SAC name	Earthquake location	Magnitude	Distance (km)	PGA (g)
50% in 50 years	LA41	Coyote Lake	5.7	8.8	0.590
	LA42	Coyote Lake	5.7	8.8	0.333
	LA43	Imperial Valley	6.5	1.2	0.144
	LA44	Imperial Valley	6.5	1.2	0.112
	LA45	Kern	7.7	107.0	0.144
	LA46	Kern	7.7	107.0	0.159
	LA47	Landers	7.3	64.0	0.338
	LA48	Landers	7.3	64.0	0.308
	LA49	Morgan Hill	6.2	15.0	0.319
	LA50	Morgan Hill	6.2	15.0	0.547
	LA51	Parkfield Cholame 5W	6.1	3.7	0.781
	LA52	Parkfield Cholame 5W	6.1	3.7	0.632
	LA53	Parkfield Cholame 8W	6.1	8.0	0.694
	LA54	Parkfield Cholame 8W	6.1	8.0	0.791
	LA55	North Palm Springs	6	9.6	0.518
	LA55	North Palm Springs	6	9.6	0.379
	LA55	San Fernando	6.5	1.0	0.253
	LA58	San Fernando	6.5	1.0	0.231
	LA59	Whittier	6	17.0	0.769
	LA60	Whittier	6	17.0	0.479

Table 4: Definitions of classical IMs

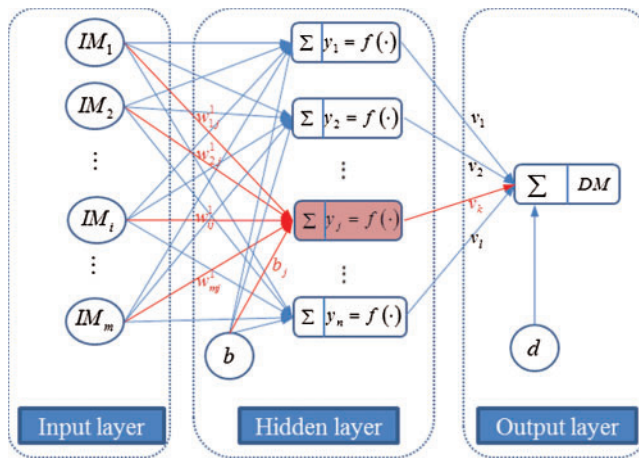
IM_i	Name	Definitions	Comments
IM_1	Peak ground acceleration (PGA)	$\max a(t) $	$a(t)$: acceleration time history
IM_2	Peak ground velocity (PGV)	$\max v(t) $	$v(t)$: velocity time history
IM_3	Peak ground displacement (PGD)	$\max u(t) $	$u(t)$: displacement time history
IM_4	Spectral acceleration (Sa)	$Sa(T_1, r_d)$	$T_1 = 4.88$, $r_d = 2$
IM_5	Average spectral acceleration (ASA)	$\frac{1}{t_2 - t_1} \int_{t_1}^{t_2} Sa(t, r_d) dt$	$t_1 = 0.2T_1$, $t_2 = 2T_1$
IM_6	Cumulative absolute velocity (CAV)	$\int_0^T a(t) dt$	T : duration
IM_7	Arias intensity (Ia)	$\frac{\pi}{2g} \int_0^T a(t) ^2 dt$	g : gravity acceleration

Table 5: Correlation coefficients between the IMs and DM in the log-log space

IM	IM_1	IM_2	IM_3	IM_4	IM_5	IM_6	IM_7
ρ	0.7677	0.9529	0.9563	0.9346	0.9754	0.7961	0.8447

Table 6: SPCCs between the IMs and DM in the log–log space

<i>IM</i>	<i>IM</i> ₁	<i>IM</i> ₂	<i>IM</i> ₃	<i>IM</i> ₄	<i>IM</i> ₅	<i>IM</i> ₆	<i>IM</i> ₇
ρ	-0.0180	0.0679	-0.0058	0.0664	0.0412	-0.0362	0.0363

**Figure 3:** The ANN model

$$f(x) = \frac{1}{1 + e^{-\alpha x}} \quad (3)$$

and can be used to model the nonlinear behavior of the ANN, in which α is the sigmoid slope which is taken as 1 herein.

Finally, the *DM* calculated in the output layer can be expressed as

$$DM = \sum_{j=1}^n v_j y_j + d \quad (4)$$

where v_j is the weight coefficient between the output and the *j*th neuron in the hidden layer and d is the bias in the output layer.

During the training of the ANN model, the discrepancy between the predicted *DM* and actual \overline{DM} is used to measure the performance of the ANN. A mean squared error (*MSE*) can typically be adopted to quantify the difference and is defined as

$$MSE = \sum_{i=1}^N (DM_i - \overline{DM}_i)^2 / N \quad (5)$$

in which N is the number of testing data, DM_i is the *i*th predicted value and \overline{DM}_i is the *i*th actual value.

Once the *MSE* is less than the pre-defined target, the training of the ANN model is terminated and an ANN regression model is built. Otherwise, the training continues and the control

parameters, e.g., the weight coefficient and bias, are updated according to a training algorithm (such as the Levenberg–Marquardt training algorithm). Subsequently, a new output is computed to examine the convergence of the system.

To improve the training efficiency of the ANN model, all input and output variables must be normalized beforehand by mapping the original values to the dimensionless range [0,1] or [−1,−1]. As the fragility analysis is conducted in the logarithmic space, the following scaled equation should be used:

$$\ln p' = \frac{\ln p - \ln \bar{p}}{\sigma} \quad (6)$$

where p' and p indicate the scaled and unscaled values, respectively; and \bar{p} and σ respectively denote the mean and logarithmic standard deviation.

2.3 ML-Based Seismic Fragility Predictions

In this section, seismic fragility analysis is performed according to ML. First, in view of the prediction uncertainty of the ANN model, an optimal regression model is chosen from many trained ones (Figs. 1e–1h). Subsequently, the input *IMs* should be determined, including the sample range and size. Finally, the *DMs* can be predicted using the optimal ANN regression model and will be used to calculate the fragility curve. The following sections discuss the sampling method of the selected *IMs* and the computation of the fragility curve.

2.3.1 Sampling Methods of Selected IMs

In ML-based seismic fragility analysis, the size of the *IMs-DM* sample data considerably affects the accuracy of the prediction. If the sample data is sufficiently large, then the failure probability of the structure under an earthquake can be accurately computed. However, the values of the *IMs* cannot be in an unlimited range [0, inf). To reasonably take these values, the statistical distributions of the selected *IMs* according to 60 earthquake waves can be used (Figs. 1d–1g). This paper adopted two sampling methods to ascertain the *IMs* using their statistical distributions: (1) truncated random distribution (TRD) and (2) truncated uniform distribution (TUD). In the former, the *IMs* are randomly taken in a specific range; whereas in the latter, the *IMs* are uniformly distributed in a given interval.

2.3.2 Computation of Fragility Curves

In this section, the MCS and *Reg* method are adopted to compute the fragility curves of the structure under an earthquake. In the ML-based MCS, all selected *IMs* for a given PGA level x can be determined using the above sampling methods and statistical distributions. Then, the *DMs* can be predicted using the ANN model, (Figs. 1g–1i). Finally, the probability of the structure reaching or exceeding the damage state D_i can be computed as [15]

$$P_{MCS}^i[DM \geq D_i | PGA = x] = \frac{1}{n} \sum_{j=1}^n \mathbf{1}[DM_j \geq D_i] \quad (7)$$

where n is the number of ground motions; DM_j is the *DM* value (i.e., maximum IDR) of the structure subjected to j th seismic motion; and $\mathbf{1}[DM_j \geq D_i]$ is 1 when $DM_j \geq D_i$ and 0 otherwise.

In the *Reg* method, the fragility of the structure or component can be expressed in a form of lognormal cumulative distributions, and the conditional probability of failure for the specific damage state D_i can be written as [10].

$$P_{\text{Reg}}^i[DM \geq D_i | PGA = x] = \Phi \left[\frac{1}{\beta_i} \ln \left(\frac{x}{\alpha_i} \right) \right] \quad (8)$$

in which Φ is the standard normal cumulative distribution function (CDF), α_i is the median value of the PGA at which the DM reaches or exceeds the threshold D_i , and β_i is the corresponding logarithmic standard deviation.

Given the limited sample data, the structure may not reach the damage state D_i when the PGA takes the maximum value in some samples. Consequently, the conventional method for computing the mean and logarithmic standard deviation is inapplicable here. In this study, a multiple stripes analysis (MSA) method is adopted, in which two parameters α_i and β_i are estimated by using the maximum likelihood method [10]. The likelihood function corresponding to the damage state D_i can be written as

$$L_i = \prod_{j=1}^m \binom{n}{z_j^i} \Phi \left(\frac{1}{\beta_i} \ln \left(\frac{x_j}{\alpha_i} \right) \right)^{z_j^i} \left[1 - \Phi \left(\frac{1}{\beta_i} \ln \left(\frac{x_j}{\alpha_i} \right) \right) \right]^{n-z_j^i} \quad (9)$$

in which m is the number of PGA levels, z_j^i is the number of ground motions at which the structure reaches or exceeds the damage state D_i at $PGA = x_j$, and \prod is a product over all PGA levels. α_i and β_i in Eq. (8) are computed as $\hat{\alpha}_i$ and $\hat{\beta}_i$ by maximizing the logarithm of the likelihood function L_i [10]. Thus,

$$\left\{ \hat{\alpha}_i, \hat{\beta}_i \right\} = \underset{\alpha_i, \beta_i}{\text{argmax}} \sum_{j=1}^m \left\{ \ln \left(\binom{n}{z_j^i} \right) + z_j^i \ln \Phi \left(\frac{1}{\beta_i} \ln \left(\frac{x_j}{\alpha_i} \right) \right) + (n - z_j^i) \ln \left[1 - \Phi \left(\frac{1}{\beta_i} \ln \left(\frac{x_j}{\alpha_i} \right) \right) \right] \right\} \quad (10)$$

3 Results and Discussions

3.1 NFES Results

In this section, the 60 ground motion records in Section 2.1.2 are selected as the seismic inputs. To increase the sample size, the PGA of each earthquake wave is scaled from 0.1 g to 1.5 g in increments of 0.1 g. Then, the IM_2 and IM_4 (shown in Tab. 4) of each record can be computed. A total of 900 $IMs-DM$ sample sets are thus generated. The damage states in terms of the DM are defined in four levels in this research: negligible (D_1), light (D_2), moderate (D_3) and severe (D_4). The corresponding threshold values are 0.5%, 1.5%, 2.5%, and 3.8%. The $PGA-DM$ cloud data calculated according to the NFES are depicted in Fig. 4. The statistical numbers of the ground motions in each PGA level when the steel BRB frame reaches or exceeds the four damage states are summarized in Tab. 7.

The two parameters in Eq. (8) at the four damage states are given in Tab. 8. In addition, the fragility curves using the NFES are plotted in Fig. 5, for which the discrete data points were computed using the MCS and the counterparts for the solid lines were obtained with the *Reg* method.

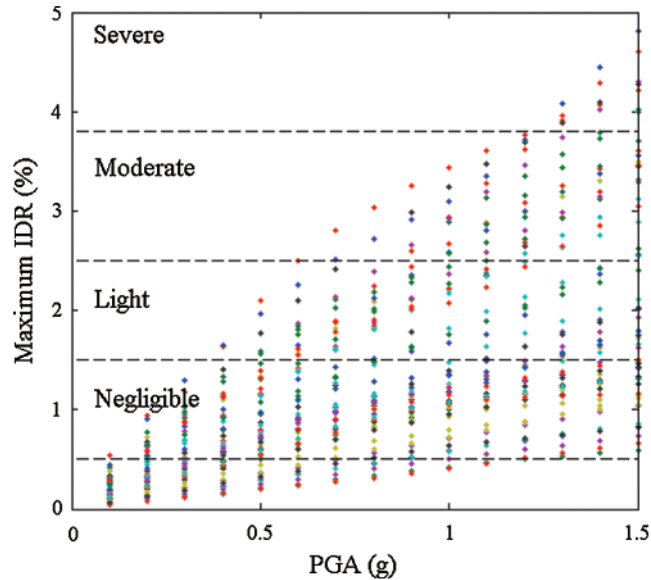


Figure 4: DM-PGA data points according to the NFES

Table 7: Number of ground motions reaching or exceeding specific damage states ($n = 60$)

PGA (g)	0.1	0.2	0.3	0.4	0.5	0.6	0.7	0.8	0.9	1	1.1	1.2	1.3	1.4	1.5
z^1	1	19	29	42	50	51	52	54	57	58	58	59	60	60	60
z^2	0	0	0	3	8	14	19	21	24	24	26	27	34	35	38
z^3	0	0	0	0	0	0	3	4	7	11	15	18	20	20	23
z^4	0	0	0	0	0	0	0	0	0	0	0	0	5	6	8

Table 8: Parameters of the fragility curves

Damage state	D_1	D_2	D_3	D_4
$\hat{\alpha}_i$	0.3059	0.6693	1.1612	1.5173
$\hat{\beta}_i$	0.6658	0.5678	0.4117	0.2594

3.2 Training and Validation of the ANN

Subsequently, the feedforward ANN model is trained using the input variables IM_2 and IM_4 (i.e., PGV and Sa) and actual output DM (i.e., maximum IDR). Given the limited sample data, a k -fold cross validation method is adopted to improve the generality of the ANN model ($k = 15$ herein), in which the 900 IMs - DM samples are randomly and equally divided into 15 subsets. Note that the ANN model is trained 15 times, and one subset is used for validation while the other 14 ones are utilized for training in each training process. Moreover, the validation subsets in any two processes vary.

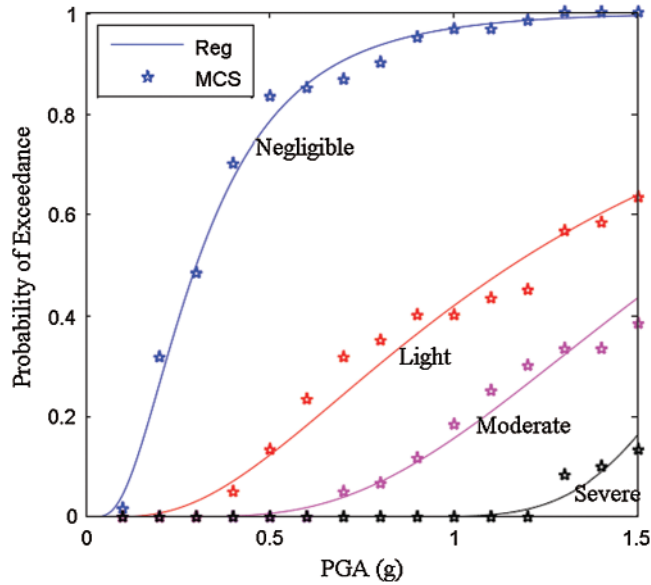


Figure 5: Fragility curves obtained using the NFES

Herein, a three-layer ANN model with six neurons is used, and the *MSE* is adopted to measure the performance of the model. The minimum *MSE* (i.e., goal of performance) is 0.001, the learning rate is 0.001, the momentum is 0.9, the epoch is 100, and the maximum validation check is 6. To overcome the overfitting, the training stops when the validation error reaches its minimum value [40] (Fig. 6).

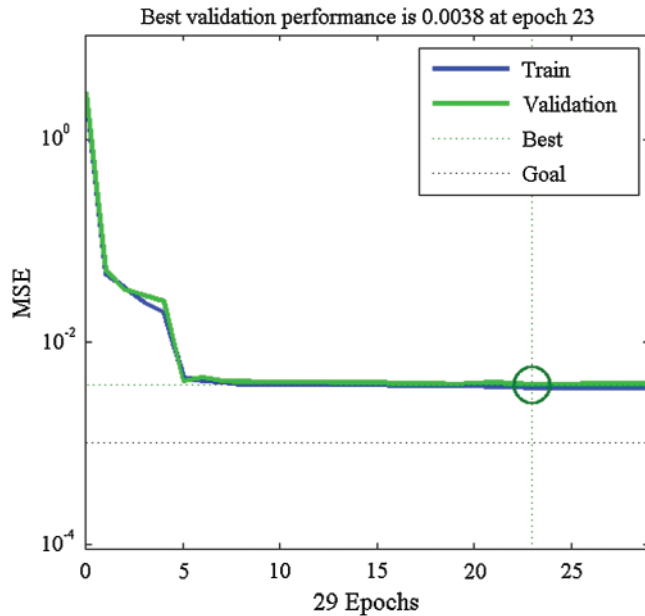


Figure 6: Early stopping of the ANN model

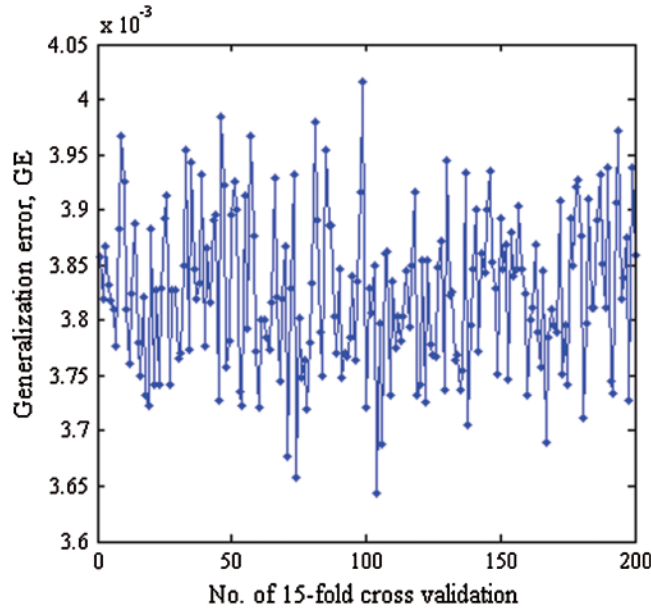


Figure 7: Generalization error of the ANN model

Given the prediction uncertainty of the ANN model, the 15-fold cross validation-based ANN is trained 200 times. The generalization error is illustrated in Fig. 7. In line with Fig. 7, the prediction uncertainty of the ANN regression model cannot be ignored. For accurate simulation, the optimal ANN regression model with a minimum error is selected, saved, and used in the following computation. The predicted IM_2 - DM and IM_4 - DM data points according to the optimal model are compared with the NFES results in Fig. 8. An acceptable discrepancy occurs between the simulations using the ANN and NFES (Fig. 8). Therefore, the accuracy and reliability of the ANN are verified.

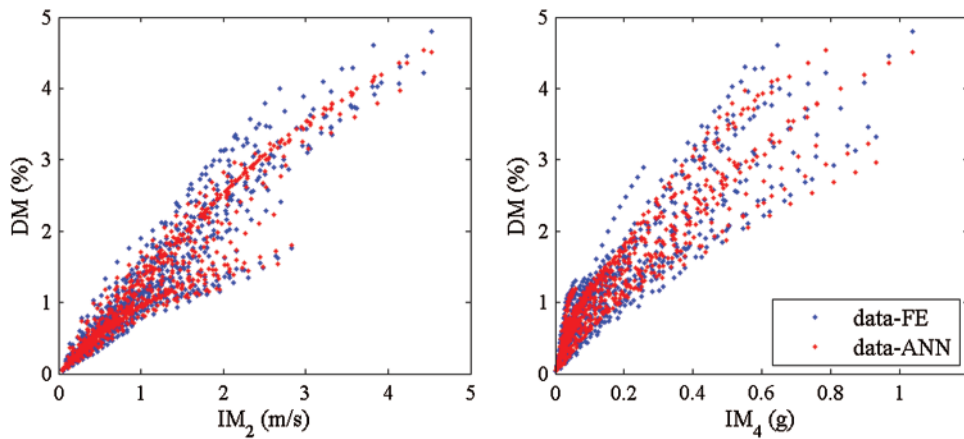


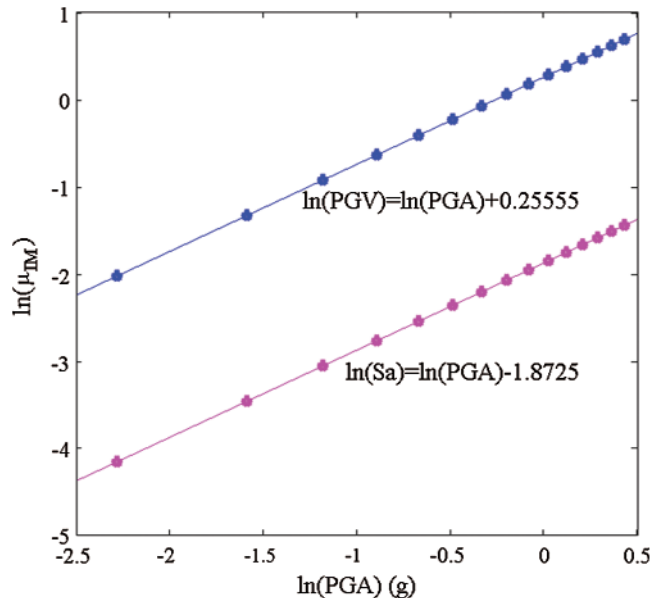
Figure 8: ANN simulations

Table 9: Statistical logarithmic means of IM_2 and IM_4

$PGA (g)$	0.1	0.2	0.3	0.4	0.5	0.6	0.7	0.8
$\ln \mu_2$	-2.027	-1.334	-0.928	-0.641	-0.417	-0.235	-0.081	0.053
$\ln \mu_4$	-4.155	-3.462	-3.056	-2.769	-2.545	-2.363	-2.209	-2.075
$PGA (g)$	0.9	1.0	1.1	1.2	1.3	1.4	1.5	
$\ln \mu_2$	0.170	0.276	0.371	0.458	0.538	0.612	0.681	
$\ln \mu_4$	-1.958	-1.852	-1.757	-1.670	-1.590	-1.516	-1.447	

3.3 ANN-Based Fragility Prediction

In Section 3.3, the fragility curves are calculated using the trained ANN model. The statistical logarithmic means of the IM_2 (PGV) and IM_4 (Sa) obtained from the 60 earthquake waves are listed in Tab. 9. The logarithmic standard deviation of the PGV and Sa (denoted as σ_2 and σ_4) for each PGA level are approximately 0.4881 and 0.9713, respectively. The means show strong linear relationships with the PGA in the log-log space (Fig. 9). The statistical distributions of the normalized logarithmic PGV and Sa at each PGA level are depicted in Fig. 10. Clearly, the PGV follows a good logarithmic normal distribution whereas the Sa does not.

**Figure 9:** Regression relationships between two selected IMs and PGA in log-log space

Subsequently, the PGA is increased from 0.1 g to 2.0 g in increments of 0.1 g (for a total 20 PGA levels) and transformed from the logarithmic space. Then, the logarithmic means $\ln \mu_2$ and $\ln \mu_4$ are calculated according to the linear regression relationships shown in Fig. 9. The logarithmic IM_2 and IM_4 at each PGA level and in accordance with the statistical distributions are shown in Fig. 10. Finally, the normalized $\ln IM'_2$ and $\ln IM'_4$ obtained from Eq. (6) are used to predict the normalized $\ln DM'$, and the fragility curve can thus be computed on the basis of the $\ln DM$. In the following sections, the effects of the sampling methods and sample

size on the fragility curve, as well as on the prediction uncertainty of the ANN model, are respectively studied.

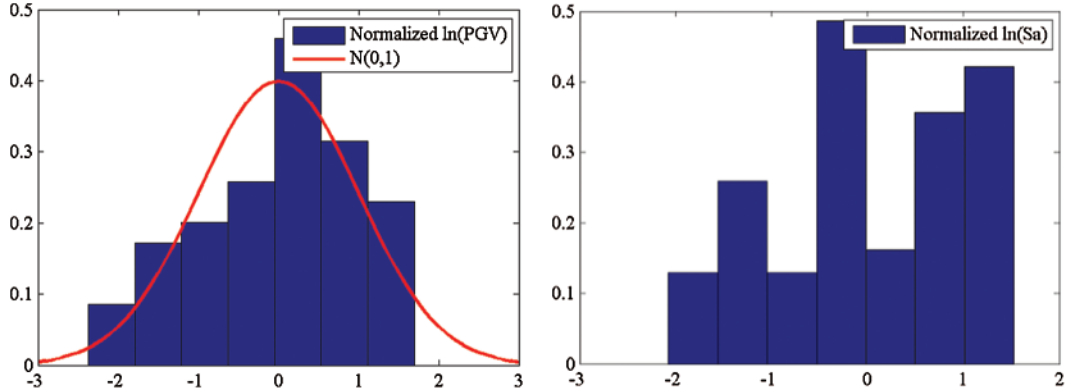


Figure 10: Statistical distributions of normalized logarithmic PGV and Sa

Case I: Comparison of TRD and TUD

According to the statistical distributions of the PGV and Sa , the TRD and TUD introduced in Section 2.3.1 are adopted to take the values of PGV and Sa . For TRD, 10000 $\ln IM_2$ and 10000 $\ln IM_4$ are randomly taken in the range of $\ln \mu_i - 2 \ln \sigma_i$ and $\ln \mu_i + 2 \ln \sigma_i$, whereas for TUD, they are uniformly distributed in $[\ln \mu_i - 2 \ln \sigma_i, \ln \mu_i + 2 \ln \sigma_i]$ with an increment of $0.01\sigma_i$. A total of 160801 data were involved. Fig. 11 shows the fragility curves using TRD and TUD. The fragility curves for the two sampling methods are almost the same (Fig. 11), but the probability of exceedance using TRD is obviously higher than that using TUD for the moderate and severe damage states. Therefore, simulation using TUD is more conservative than that using TRD. TUD is consequently adopted in the following analyses.

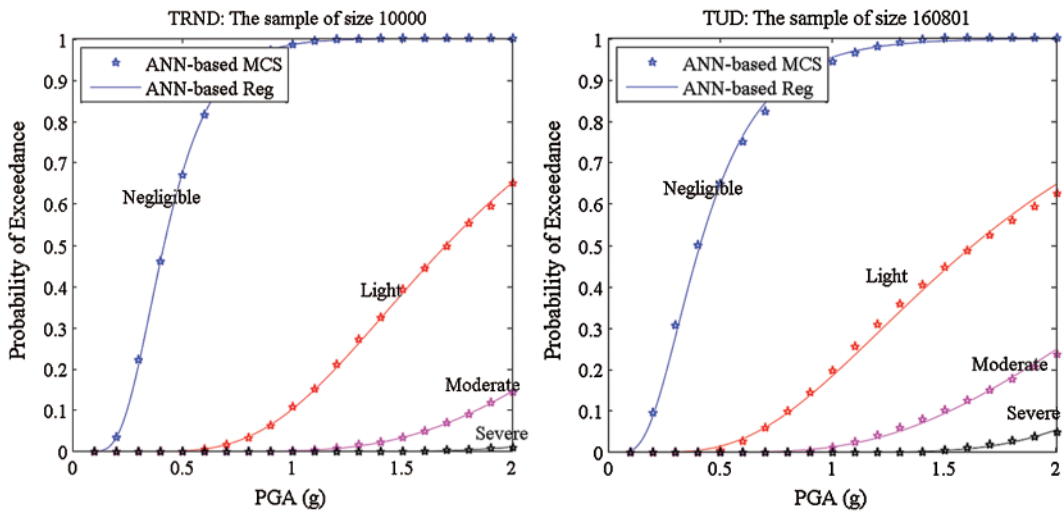


Figure 11: Fragility curves using different distributions of IMs. (a) TRD and (b) TUD

Case II: Effect of sample size

Herein, the effect of sample size on the fragility curve is studied. Fig. 12 presents the results of TUD using four sample sizes of 1681, 6561, 40401, and 160801. The maximum relative errors for those values are listed in Tab. 10. Fig. 12 and Tab. 10 indicate that the results of the MCS and Reg method using various sample sizes are very close to each other, and the relative maximum error decreases when the sample size increases. Furthermore, sample size has a slight influence on the fragility. In this study, TUD with a sample size of 1681 can provide a reasonable and acceptable prediction.

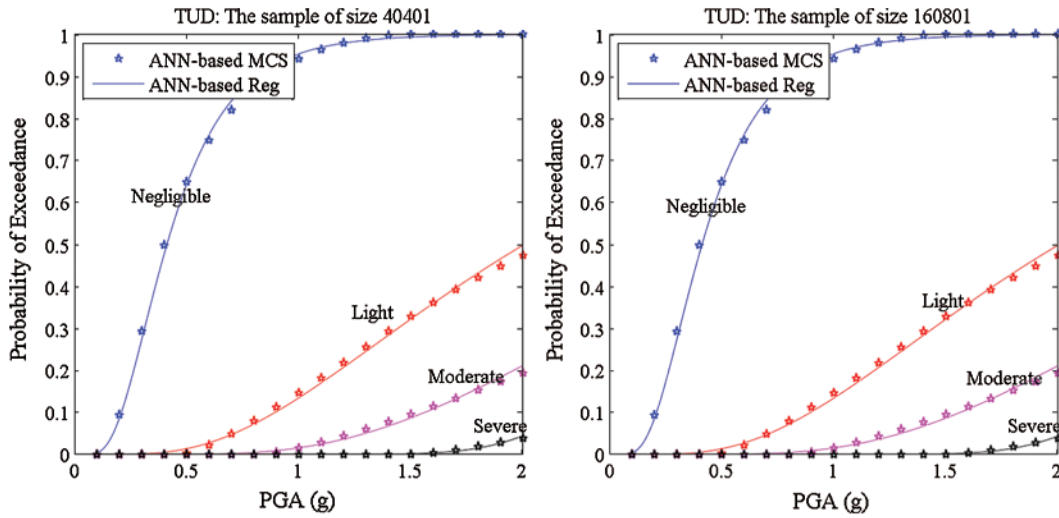


Figure 12: Effect of sample size on fragility curves using TUD

Table 10: Maximum relative error between the results using the TUD with various sample sizes

Damage state	D_1	D_2	D_3	D_4
$e_{1681 6561}(\%)$	0.3692	0.3490	0.3415	0.2594
$e_{6561 40401}(\%)$	0.2225	0.1645	0.1714	0.1452
$e_{40401 160801}(\%)$	0.0642	0.0570	0.0539	0.0454

Case III: Investigation of the prediction uncertainty

In this section, the prediction uncertainties of the ANN model are discussed, for which the variability of the output is illustrated in Fig. 7. Herein, the effects of the input *IMs* range, as well as the training and validation ratios, on the fragility curve are investigated. Fig. 13 depicts the fragility curves using three various *IMs* ranges, i.e., $[\ln \mu_i - 1.5\sigma_i, \ln \mu_i + 1.5\sigma_i]$, $[\ln \mu_i - 2.0\sigma_i, \ln \mu_i + 2.0\sigma_i]$, and $[\ln \mu_i - 2.5\sigma_i, \ln \mu_i + 2.5\sigma_i]$. As evident from Fig. 7, as the value range of the *IMs* increases, the probabilities of exceedance at the four damage states increase at the low *PGA* levels, and decrease at the high *PGA* levels. Further, prediction uncertainties due to the training and validation ratios are studied. The outcomes of three simulations using the 10-, 15-, and 20-fold cross validation methods are given in Tab. 11 and their influences on the fragility curves are depicted in Fig. 14.

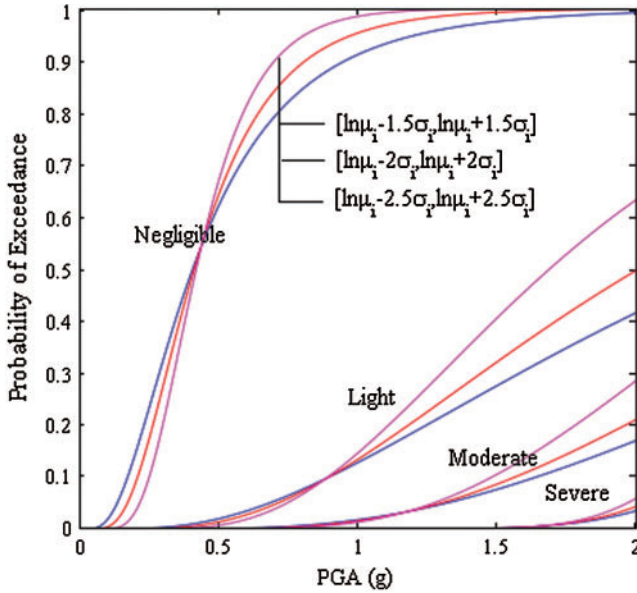


Figure 13: Effect of the range of IMs on fragility curves

The above analyses indicate that the prediction uncertainties of the ANN model cannot be ignored. In particular, the value range of the *IMs* exerts a considerable effect on the fragility analysis. The training and validation ratios have slight influences on the fragility curves of the structure at the negligible and severe damage states, whereas they have noticeable effects given light and moderate damage states.

Table 11: Three train cases using various ratios for training, validation, and testing

No.	Method	Train ratio	Validation ratio	Minimum MSE
Train 1	10-fold cross validation	9/10	1/10	0.00363
Train 2	15-fold cross validation	14/15	1/15	0.00364
Train 3	20-fold cross validation	19/20	1/20	0.00364

3.4 Computational Cost

Finally, the time costs of the fragility analyses using the NFES and ANN are summarized in Tab. 12. In this study, all computations are conducted on a HP Workstation with an Inter Xeon W-2155 CPU with 10 physical cores at 3.3 GHz, and 64 GB of RAM. As the FE model is large scale, complex, and entails a substantial matrix size, the NFES uses a six-processor parallel method and requires approximately 2380 h. By contrast, the trainings of the ANN model based on the 10, 15, and 20-fold cross validation methods merely require approximately 8, 13, and 15 min, respectively. Furthermore, the time cost of the prediction using the ANN model in Section 3.3 is only 2 min. Therefore, the ANN model exhibits extremely high computational efficiency.

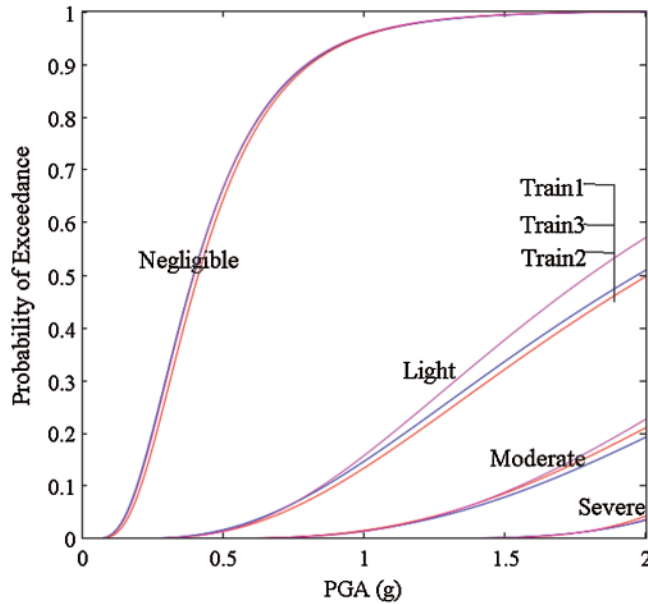


Figure 14: Effect of training and validation ratios on fragility curves

Table 12: Comparisons of computational costs using NFES and ANN

Type of analyses	No. of samples	Total time cost
FE simulation	900	2380 h
10-fold cross validation	180000	8 min
15-fold cross validation	180000	13 min
20-fold cross validation	180000	15 min
ANN prediction	10529490	2 min

4 Conclusions

In this paper, a machine learning (ML)-based seismic fragility analysis framework is presented to examine the failure probability of a realistic large-scale steel BRB frame under earthquakes. The framework consists of a few sequential steps: building the model for nonlinear finite element simulation (NFES), training and validating an artificial neural network (ANN) model, and performing the fragility analysis using the ANN model. In the NFES, 60 earthquake records are selected and a total of 900 sample data can be generated by scaling the peak ground acceleration (PGA) of each record from 0.1 g to 1.5 g in increments of 0.1 g. The damage measures (DMs) of the structure, such as the maximum inter-story drift ratios, under these ground motions, are computed based on the NFES. Subsequently, the two most relevant IMs (i.e., PGV and Sa) with the DM are filtered by using the semi-partial correlation coefficient and an optimal ANN model is obtained using the IMs - DM data. The extended IMs from using the two sampling methods are inputted to the optimal ANN model to compute the DMs . Then, the fragility curves are

calculated using the Monte Carlo Simulation and empirical regression method. The following conclusions can be obtained through the simulations:

- (1) The ML-based seismic fragility analysis framework is of significantly high computational efficiency and can instantaneously assess the failure risk of a large-scale structure under an earthquake. The trained ANN regression model based on the two *IMs* (i.e., *PGV* and *Sa*) and *DM* is reliable and accurate.
- (2) The truncated uniform sampling method outperforms the truncated random one. The two methods have almost similar fragility curves of the steel BRB frame at the negligible and light damage states. However, the result of truncated uniform sampling is slightly more reliable than that of its random counterpart at the moderate and severe damage states. In addition, the former is not sensitive to sample size.
- (3) The prediction uncertainties of the ANN cannot be ignored. The truncated ranges of *IMs* have considerable influences on the fragility curves, and the training and validation ratios also show notable effects on the probabilities of exceedance of the structure at the light and moderate damage states.

Funding Statement: Financial support received from the Scientific Research Fund of Institute of Engineering Mechanics, China Earthquake Administration under Grant No. 2019EEEVL05, the National Key Research and Development Program of China under Grant No. 2016YFC0701106, the National Natural Science Foundation of China under Grant No. 51578473 are gratefully acknowledged.

Conflicts of Interest: The authors declare that they have no conflicts of interest to report regarding the present study.

References

1. Bai, J., Cheng, F., Jin, S., Ou, J. (2019). Assessing and quantifying the earthquake response of reinforced concrete buckling-restrained brace frame structures. *Bulletin of Earthquake Engineering*, 17(7), 3847–3871. DOI 10.1007/s10518-019-00633-0.
2. Bai, J., Ou, J. (2016). Earthquake-resistant design of buckling-restrained braced RC moment frames using performance-based plastic design method. *Engineering Structures*, 107, 66–79. DOI 10.1016/j.engstruct.2015.10.048.
3. Du, K., Cheng, F., Bai, J., Jin, S. (2020). Seismic performance quantification of buckling-restrained braced RC frame structures under near-fault ground motions. *Engineering Structures*, 211, 110–447. DOI 10.1016/j.engstruct.2020.110447.
4. Sutcu, F., Takeuchi, T., Matsui, R. (2014). Seismic retrofit design method for RC buildings using buckling-restrained braces and steel frames. *Journal of Constructional Steel Research*, 101, 304–313. DOI 10.1016/j.jcsr.2014.05.023.
5. Güneyisi, E. M. (2012). Seismic reliability of steel moment resisting framed buildings retrofitted with buckling restrained braces. *Earthquake Engineering & Structural Dynamics*, 41(5), 853–874. DOI 10.1002/eqe.1161.
6. Ellingwood, B. R. (2001). Earthquake risk assessment of building structures. *Reliability Engineering & System Safety*, 74(3), 251–262. DOI 10.1016/S0951-8320(01)00105-3.
7. Smith, M. A., Caracoglia, L. (2011). A Monte Carlo based method for the dynamic fragility analysis of tall buildings under turbulent wind loading. *Engineering Structures*, 33(2), 410–420. DOI 10.1016/j.engstruct.2010.10.024.

8. Gehl, P., Douglas, J., Seyedi, D. M. (2015). Influence of the number of dynamic analyses on the accuracy of structural response estimates. *Earthquake Spectra*, 31(1), 91–113. DOI 10.1193/102912EQS320M.
9. Shinozuka, M., Feng, M. Q., Lee, J., Naganuma, T. (2000). Statistical analysis of fragility curves. *Journal of Engineering Mechanics*, 126(12), 1224–1231. DOI 10.1061/(ASCE)0733-9399(2000)126:12(1224).
10. Baker, J. W. (2015). Efficient analytical fragility function fitting using dynamic structural analysis. *Earthquake Spectra*, 31(1), 579–599. DOI 10.1193/021113EQS025M.
11. Cardoso, J. B., de Almeida, J. R., Dias, J. M., Coelho, P. G. (2008). Structural reliability analysis using Monte Carlo simulation and neural networks. *Advances in Engineering Software*, 39(6), 505–513. DOI 10.1016/j.advengsoft.2007.03.015.
12. Chen, G., Li, T., Chen, Q., Ren, S., Wang, C. et al. (2019). Application of deep learning neural network to identify collision load conditions based on permanent plastic deformation of shell structures. *Computational Mechanics*, 64(2), 435–449. DOI 10.1007/s00466-019-01706-2.
13. Cheng, J., Li, Q. S. (2008). Reliability analysis of structures using artificial neural network based genetic algorithms. *Computer Methods in Applied Mechanics and Engineering*, 197(45), 3742–3750. DOI 10.1016/j.cma.2008.02.026.
14. Cheng, J., Li, Q. S., Xiao, R. (2008). A new artificial neural network-based response surface method for structural reliability analysis. *Probabilistic Engineering Mechanics*, 23(1), 51–63. DOI 10.1016/j.probengmech.2007.10.003.
15. Deng, J., Gu, D., Li, X., Yue, Z. Q. (2005). Structural reliability analysis for implicit performance functions using artificial neural network. *Structural Safety*, 27(1), 25–48. DOI 10.1016/j.strusafe.2004.03.004.
16. Goh, A. T., Kulhawy, F. H. (2003). Neural network approach to model the limit state surface for reliability analysis. *Canadian Geotechnical Journal*, 40(6), 1235–1244. DOI 10.1139/t03-056.
17. Gomes, H. M., Awruch, A. M. (2004). Comparison of response surface and neural network with other methods for structural reliability analysis. *Structural Safety*, 26(1), 49–67. DOI 10.1016/S0167-4730(03)00022-5.
18. Hosni Elhewy, A., Mesbahi, E., Pu, Y. (2006). Reliability analysis of structures using neural network method. *Probabilistic Engineering Mechanics*, 21(1), 44–53. DOI 10.1016/j.probengmech.2005.07.002.
19. Huang, C. S., Hung, S. L., Wen, C. M., Tu, T. T. (2003). A neural network approach for structural identification and diagnosis of a building from seismic response data. *Earthquake Engineering & Structural Dynamics*, 32(2), 187–206. DOI 10.1002/eqe.219.
20. Papadrakakis, M., Papadopoulos, V., Lagaros, N. D. (1996). Structural reliability analysis of elastic-plastic structures using neural networks and Monte Carlo simulation. *Computer Methods in Applied Mechanics and Engineering*, 136(1), 145–163. DOI 10.1016/0045-7825(96)01011-0.
21. Richard, B., Cremona, C., Adelaide, L. (2012). A response surface method based on support vector machines trained with an adaptive experimental design. *Structural Safety*, 39, 14–21. DOI 10.1016/j.strusafe.2012.05.001.
22. Wang, Y., Wang, C., Li, H., Zhao, R. (2009). Artificial neural network prediction for seismic response of bridge structure. *International Conference on Artificial Intelligence and Computational Intelligence*, pp. 503–506. Shanghai, China.
23. Yan, W., Deng, L., Zhang, F., Li, T., Li, S. (2019). Probabilistic machine learning approach to bridge fatigue failure analysis due to vehicular overloading. *Engineering Structures*, 193, 91–99. DOI 10.1016/j.engstruct.2019.05.028.
24. Calabrese, A., Lai, C. G. (2013). Fragility functions of blockwork wharves using artificial neural networks. *Soil Dynamics and Earthquake Engineering*, 52, 88–102. DOI 10.1016/j.soildyn.2013.05.002.
25. Zio, E. (2006). A study of the bootstrap method for estimating the accuracy of artificial neural networks in predicting nuclear transient processes. *IEEE Transactions on Nuclear Science*, 53(3), 1460–1478. DOI 10.1109/TNS.2006.871662.

26. Ferrario, E., Pedroni, N., Zio, E., Lopez-Caballero, F. (2015). Application of metamodel-based techniques for the efficient seismic analysis of structural systems. *Safety and Reliability of Complex Engineered Systems*, pp. 1193–1200. *ESREL*, Zurich, Switzerland.
27. Ferrario, E., Pedroni, N., Zio, E., Lopez-Caballero, F. (2017). Bootstrapped artificial neural networks for the seismic analysis of structural systems. *Structural Safety*, 67, 70–84. DOI 10.1016/j.strusafe.2017.03.003.
28. Lagaros, N. D., Fragiadakis, M. (2007). Fragility assessment of steel frames using neural networks. *Earthquake Spectra*, 23(4), 735–752. DOI 10.1193/1.2798241.
29. Lagaros, N. D., Tsompanakis, Y., Psarropoulos, P. N., Georgopoulos, E. C. (2009). Computationally efficient seismic fragility analysis of geostructures. *Computers & Structures*, 87(19), 1195–1203. DOI 10.1016/j.compstruc.2008.12.001.
30. Liu, Z., Zhang, Z. (2018). Artificial neural network based method for seismic fragility analysis of steel frames. *KSCE Journal of Civil Engineering*, 22(2), 708–717. DOI 10.1007/s12205-017-1329-8.
31. Mitropoulou, C. C., Papadrakakis, M. (2011). Developing fragility curves based on neural network IDA predictions. *Engineering Structures*, 33(12), 3409–3421. DOI 10.1016/j.engstruct.2011.07.005.
32. Wang, Z., Pedroni, N., Zentner, I., Zio, E. (2018). Seismic fragility analysis with artificial neural networks: application to nuclear power plant equipment. *Engineering Structures*, 162, 213–225. DOI 10.1016/j.engstruct.2018.02.024.
33. GB 50011-2010 (2010). *Code for seismic design of buildings*. China: Building Industry Press (In Chinese).
34. Mckenna, F. T. (1997). *Object-oriented finite element programming: frameworks for analysis, algorithms and parallel computing (Ph.D. Thesis)*. University of California, Berkeley, California.
35. Sun, B., Gu, Q., Zhang, P., Ou, J. (2017). A practical numerical substructure method for seismic nonlinear analysis of tall building structures. *Structural Design of Tall and Special Buildings*, 26(16), 1377. DOI 10.1002/tal.1377.
36. Sun, B., Gu, Q., Zhang, P., Li, Y., Ou, J. (2019). Efficient simulation of RC shear walls in high-rise buildings using a practical multi-cross-line-model. *Journal of Earthquake Engineering*, 91(4), 1–30. DOI 10.1080/13632469.2019.1597785.
37. FEMA (2000a). *State of the art report on systems performance of steel moment frames subject to earthquake ground shaking*. Washington, DC: FEMA.
38. FEMA (2000b). *Prestandard and commentary for the seismic rehabilitation of buildings*. Washington, DC: FEMA.
39. Riddell, R. (2007). On ground motion intensity indices. *Earthquake Spectra*, 23(1), 147–173. DOI 10.1193/1.2424748.
40. Lee, C., Overfitting, G., Caruana, R., Lawrence, S., Giles, L. (2001). Overfitting in neural nets: backpropagation, conjugate gradient, and early stopping. *Advances in Neural Information Processing Systems 13: Proceedings of the 2000 Conference*, pp. 402–408. Cambridge, MA: MIT Press, 13.